

Physical Properties and HI-to-H₂ Transition across Taurus Linear Edge

NINGYU TANG,¹ FEIHANG MIAO,¹ GAN LUO,² DI LI,^{3,4,5} JUNZHI WANG,⁶ FUJUN DU,^{7,8} DONGHONG WU,¹ AND SHU LIU⁴

¹*Department of Physics, Anhui Normal University, Wuhu, Anhui 241002, China*

²*Institut de Radioastronomie Millimétrique, 300 rue de la Piscine, 38400, Saint-Martin d'Hères, France*

³*New Cornerstone Science Laboratory, Department of Astronomy, Tsinghua University, Beijing 100084, China*

⁴*National Astronomical Observatories, CAS, Beijing 100012, People's Republic of China*

⁵*Zhejiang Lab, Hangzhou, Zhejiang 311121, China*

⁶*Guangxi Key Laboratory for Relativistic Astrophysics, Department of Physics, Guangxi University, Nanning 530004, PR China*

⁷*Purple Mountain Observatory and Key Laboratory of Radio Astronomy, Chinese Academy of Sciences, Nanjing 210023, China*

⁸*School of Astronomy and Space Science, University of Science and Technology of China, Hefei 230026, China*

ABSTRACT

Studying the atomic-to-molecular transition is essential for understanding the evolution of interstellar medium. The linear edge of Taurus molecular cloud, clearly identified in the ¹³CO(1-0) intensity map, serves as an ideal site for investigating this transition. Utilizing the Arizona Radio Observatory Sub-Millimeter Telescope, we obtained mapping observations of CO(2-1), ¹³CO(2-1), and CO(3-2) across this linear edge. The intensity ratio between CO(2-1) and ¹³CO(2-1) indicates a lower limit of the ¹²C/¹³C ratio of 54 ± 17 . Based on multi-transition observations of CO and ¹³CO, we performed Markov Chain Monte Carlo (MCMC) fit of the physical properties across this edge using non-Local Thermodynamic Equilibrium analysis with the RADEX code, based on the Large velocity Gradient (LVG) assumption. The number density profile exhibits a pronounced jump coinciding with the H₂ infrared emission peak. The cold HI gas within the molecular cloud, manifested as HI-Narrow Self-Absorption (HINSA) features, is detected along the cloud edge. Our quantitative comparison with numerical simulations provides tentative evidence that shocks induced by colliding gas flows may contribute to the atomic-to-molecular phase transition observed along the linear edge.

Keywords: ISM: clouds — ISM: evolution — ISM: molecules.

1. INTRODUCTION

The transition from HI gas to H₂ gas is considered a critical process for understanding the evolution of star formation. Photo-dominated regions (e.g., PDRs, [Hollenbach & Tielens 1999](#); [Snow & McCall 2006](#)), which are dominated by far-ultraviolet (FUV; $6 \text{ eV} \lesssim h\nu \lesssim 13.6 \text{ eV}$) photons, maintain a natural atomic-molecular transition between warm HI envelope and cold H₂ center. The in situ formation of CO has been detected within the warm HI envelope (with an excitation temperature of $\sim 100 \text{ K}$) located at the boundary of supershells (e.g., [Dawson et al. 2011, 2015](#)). In the center of the molecular cloud where FUV photons are well shielded, cold HI gas with a kinetic temperature of ~ 10

K can exist (e.g., [Heiles 1969](#); [Li & Goldsmith 2003](#)). The cold HI arises from the dissociation of H₂ by low-energy cosmic rays (LECRs). Understanding the physical conditions that govern atomic-to-molecular transition inside the molecular cloud is also of paramount scientific interest.

With ¹³CO(1-0) data, a clear ‘linear edge’ was observed toward the boundary of Taurus molecular cloud ([Goldsmith et al. 2008](#)). It provides an ideal site for investigating the molecular-to-atomic transition. Toward this linear edge, [Goldsmith et al. \(2010\)](#) obtained direct H₂ infrared emission with the *Spitzer Space Telescope* and revealed the presence of warm H₂ with low column density, $(1 - 5) \times 10^{18} \text{ cm}^{-2}$. Additional heating sources, such as the dissipation of turbulence are necessary to explain this ([Goldsmith et al. 2010](#)). Based on multiple spectral observations (CII, CI, CO(1-0) and ¹³CO(1-0)), [Orr et al. \(2014\)](#) modeled this region with a

cylindrical PDR under low FUV intensity, $\chi \sim 0.05 G_0$, through combining the chemical PDR model (*Meudon*) and radiative transfer code (*RATTRAN*). With the density profile from [Orr et al. \(2014\)](#), [Xu et al. \(2016\)](#) and [Xu & Li \(2016\)](#) utilized OH and CH emissions to obtain the fraction of CO-dark molecular gas across this edge. However, the above modeling physical conditions depend on the assumption of chemical abundances ([Orr et al. 2014](#)).

The combination of multiple- J CO transitions provides a better solution in deriving physical conditions of molecular clouds. For instance, with assumption of optically thin emission and kinetic temperature of 10 K, the critical density n_{crit} of CO(3-2) is $4 \times 10^4 \text{ cm}^{-3}$, which is much larger than that of CO(1-0) ($\sim 2 \times 10^3 \text{ cm}^{-3}$) and CO(2-1) ($\sim 1 \times 10^4 \text{ cm}^{-3}$) ([Scoville et al. 1987](#)). The critical density of CO(1-0) and CO(2-1) can be reduced to $\sim 10^2 - 10^3 \text{ cm}^{-3}$ if optical depth is included. Thus the combination of multiple CO transitions is useful to determine both kinetic temperature and volume density. With the Arizona Radio Observatory Sub-Millimeter Telescope (SMT), CO surveys in multiple low- J transitions are able to derive physical conditions toward nearby molecular clouds (W51, NGC 1333, SH2-235, and Cep B/C) ([Bieging et al. 2010, 2014, 2016, 2018](#)). In diffuse region, CO excitation can not reach local thermodynamic equilibrium (LTE) and requires non-LTE analysis.

In observations, the HI Narrow Self-Absorption (HINSA) feature is considered to arise from cold ($T \sim 10 \text{ K}$) atomic hydrogen mixed with molecular gas with visual extinction $A_V > 1 \text{ mag}$ ([Li & Goldsmith 2003](#)), where FUV radiation can be well-shielded and ionization process of low-energy cosmic rays dominate. The HINSA feature, with same central velocity as CO emission, appears across this linear edge. Analyzing molecular-to-atomic transition across this edge would benefit in constraining the insitu flux of low-energy cosmic rays.

In this study, we focus on exploring the physical properties and the atomic-to-molecular transition across the Taurus linear edge. We detail the observations and archival data in Section 2, while the analysis and results concerning physical properties and HINSA column density are outlined in Section 3. Discussions regarding the results are provided in Section 4, and a concise summary is presented in Section 5.

2. OBSERVATIONS AND ARCHIVAL DATA

2.1. Observation Targets

As shown in Fig. 1, we focus on the variation of physical properties across the Taurus linear edge. We select

a total of 20 positions, of which 17 positions (P1 to P7) are the same as those in [Xu et al. \(2016\)](#) and [Xu & Li \(2016\)](#). In order to explore physical properties in extended regions, we included 3 more positions (EP1, EP2 and EP3). The separation between two nearby positions is $3'$. The intensity peak of H_2 is located in the middle of P6 and P7 ([Goldsmith et al. 2010](#)) while the peak of $^{13}\text{CO}(1-0)$ intensity is located between P9 and P10 ([Goldsmith et al. 2008](#)).

2.2. $J=2-1$ and $J=3-2$ Transitions of CO

The $J=2-1$ transitions of CO (centered at 230.538 GHz) and ^{13}CO (centered at 220.39868420 GHz) were obtained in November 2022 with 1.3 mm receiver of the SMT. The beam size is $\sim 33''$ for CO(2-1) and $\sim 35''$ for $^{13}\text{CO}(2-1)$. We adopted the On the Fly (OTF) mapping mode to cover a map with size of $5' \times 3'$ (along R.A and Dec. direction) around each position. Typical system temperature ranged between 200 and 275 K during observations. We choose backend with 64 MHz bandwidth and channel spacing of 250 kHz corresponding to velocity of $\sim 0.33 \text{ km s}^{-1}$ at 230 GHz.

The $J=3-2$ transitions of CO (centering at 345.796 GHz) were obtained in February and March 2024 with 0.8 mm receiver of the SMT. Due to time constraints, obtained map around each position has a size of $3' \times 3'$ (along R.A and Dec. direction) except P2, which has a size of $5' \times 3'$. The beam size is $\sim 22''$ for CO(3-2). The system temperature ranged from 700 to 1500 K depending on elevation angle and weather condition during observations. Selected channel spacing of 250 kHz provides velocity of $\sim 0.22 \text{ km s}^{-1}$ at 345 GHz.

Data reduction was performed with the *CLASS* program in GILDAS package¹. Bad scans with invalid values were first flagged. All reduced maps were combined together into one map by coordinate. With pixel sampling of $4''$, final root-mean-square of the spectrum of each pixel (in T_A unit) is $\sim 0.14 \text{ K}$ per 0.33 km s^{-1} for CO(2-1) and $^{13}\text{CO}(2-1)$, while it is $\sim 0.68 \text{ K}$ per 0.22 km s^{-1} for CO(3-2). The intensity map of these transition lines integrated over the velocity range -15 to 15 km s^{-1} can be found in Fig. 2.

The antenna temperature T_A^* is converted to main beam brightness temperature T_{mb} using $T_{\text{mb}} = T_A^*/\eta_{\text{eff}}$, where an efficiency factor $\eta_{\text{eff}} = 0.70$ was adopted for 1.3mm receiver, and $\eta_{\text{eff}} = 0.62$ for the 0.8mm receiver². The half-power beamwidth of SMT is $34''$ at 230 GHz, $36''$ at 220 GHz and $23''$ at 345 GHz.

¹ <https://www.iram.fr/IRAMFR/GILDAS/>

² <https://aro.as.arizona.edu/?q=beam-efficiencies>

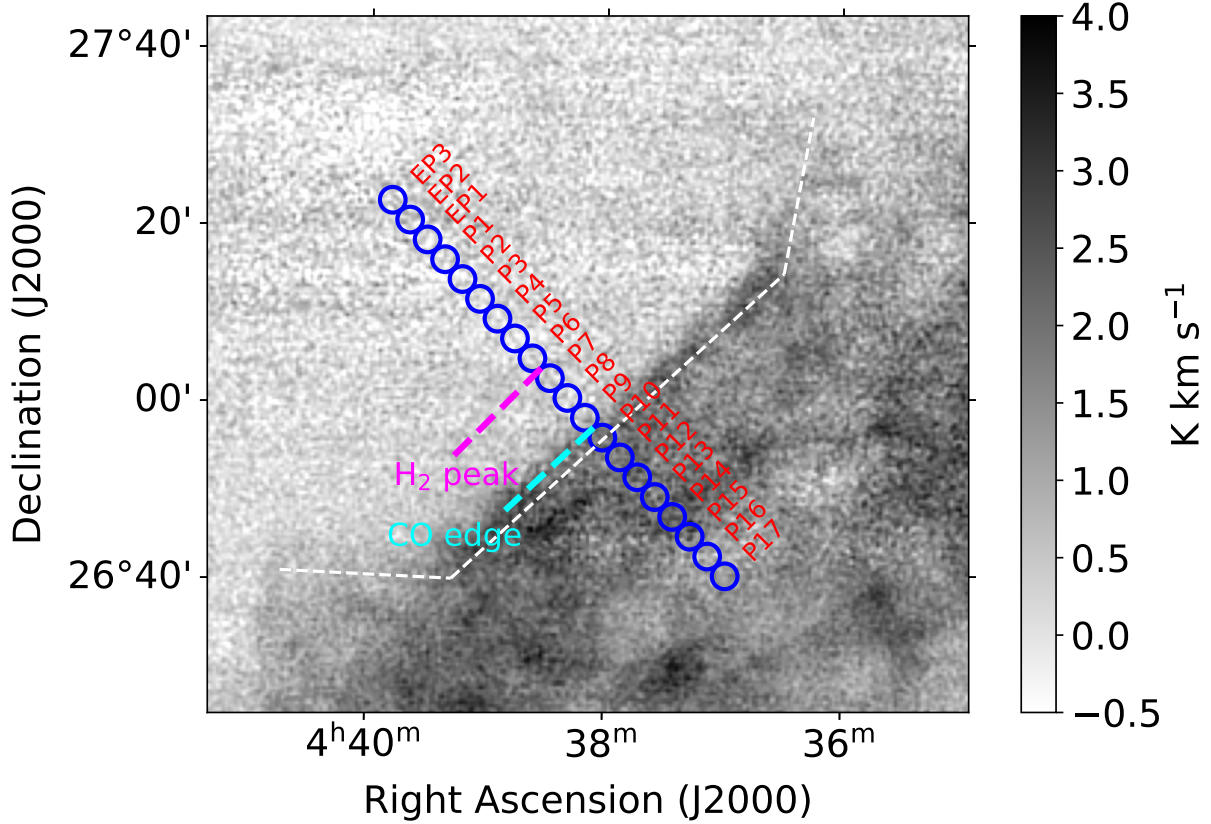


Figure 1. Spatial distribution of 20 positions (blue circles) overlaid on ^{13}CO intensity map across the Taurus linear edge. Blue circles represent observation targets with beam size of 3 arcmin. The peak intensity of the $S(0)$ and $S(1)$ transitions of H_2 locates between P6 and P7 (Goldsmith et al. 2010). Apparent CO cloud edge locates between P9 and P10. The presence of a U-shape is marked with white dashed lines.

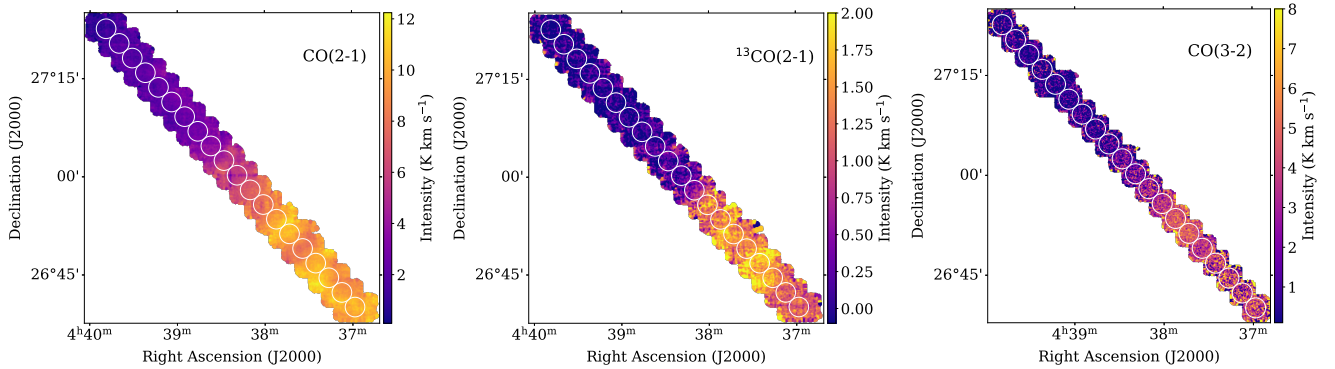


Figure 2. Obtained intensity of $\text{CO}(2-1)$, $^{13}\text{CO}(2-1)$ and $\text{CO}(3-2)$ integrated over -15 to 15 km s^{-1} across the linear edge. The white circles represent 20 positions with beam size of $3'$.

2.3. $\text{CO}(1-0)$ Data

The ^{12}CO (1-0) (centering at 115.271 GHz) and ^{13}CO (1-0) (centering at 110.201 GHz) observations were taken with the 14 m diameter millimeter-wavelength telescope of Five College Radio Astronomy Observatory (FCRAO) between 2003 and 2005. The observations have full width at half-maximum of $45''$ for ^{12}CO and

$47''$ for ^{13}CO (Narayanan et al. 2008). Main beam efficiency of 0.45 and 0.50 were used to convert antenna temperature to main beam brightness temperature of $\text{CO J}=1-0$ and $^{13}\text{CO J}=1-0$, respectively (Goldsmith et al. 2008). The data (in unit of T_{mb}) have a mean rms of 0.62 K and 0.25 K per 0.26 and 0.27 km s^{-1} for ^{12}CO and ^{13}CO , respectively.

The signal-to-noise ratio of the $^{13}\text{CO}(1-0)$ emission from EP3 to P3 is relatively low. To enhance sensitivity at these 6 positions, new $^{13}\text{CO}(1-0)$ mapping observations were taken with the Delingha 13.7m telescope between January 10th and 12th, 2025, covering an area of $22' \times 10'$. Simultaneously, corresponding $^{12}\text{CO}(1-0)$ mapping data were also obtained. The system temperature was ~ 150 K for $^{13}\text{CO}(1-0)$ and ~ 250 K for $^{12}\text{CO}(1-0)$ observations. The spectral resolution of 61 kHz corresponds to a velocity resolution of 0.17 km s^{-1} at 110.201 GHz. The sampling size of the map is $24.5''$, which is half the main beam size of the Delingha 13.7m telescope at 110.201 GHz. After processing with *GILDAS* software, rms of the spectrum (in unit of T_{mb}) for each pixel reaches 0.12 K for ^{12}CO and 0.08 K for ^{13}CO , corresponding to velocity resolutions of 0.16 and 0.17 km s^{-1} , respectively.

The peak values of $^{12}\text{CO}(1-0)$ emissions from EP3 to P3 differ by 5% to 15% between FCRAO and Delingha 13.7m observations, attributed to uncertainties in main-beam efficiency. To ensure data consistency across the 20 positions, the $^{13}\text{CO}(1-0)$ data from Delingha 13.7m were adjusted by multiplying with the peak intensity ratio of $^{12}\text{CO}(1-0)$ between FCRAO and Delingha 13.7m observations.

2.4. Archival HI Data

HI data across this linear edge were extracted from the Data Release 2 of Galactic Arecibo L-Band Feed Array HI (GALFA-HI) survey, which provides angular resolution of $\sim 4'$ and spectral sensitivity of ~ 150 mK (brightness temperature) per 1 km s^{-1} (Peek et al. 2018).

2.5. Archival E(B-V) Data

We adopted the three-dimensional (3D) dust reddening E(B-V) map from Green et al. (2019), which is based on Gaia parallaxes and stellar photometry from Pan-STARRS 1 and 2MASS. This 3D E(B-V) map has a spatial resolution of $3.4' - 13.7'$ and covers 120 distance bins from 63 pc to 63 kpc. The E(B-V) value of each position in this study was adopted as cumulative value with distance of 300 pc, which is far enough to include the Taurus molecular cloud (~ 140 pc, Palmeirim et al. 2013) and sufficient stars for calculation. The E(BV) values within a 300 pc truncation exceed 90% of those measured along the entire sightline.

3. ANALYSIS AND RESULTS

3.1. Spectral Properties

To mitigate the impact of varying spatial resolutions in observations, the multi-transitions of CO data were convolved to a beam width of $3'$ to match the spatial separation of two nearby positions.

Spectra of CO and ^{13}CO transitions are shown in Fig 3. We adopted Gaussian fitting for all spectra. One Gaussian component was used for positions EP3 to P13, whereas two components were employed for positions P14 to P17. Fitted parameters are shown in Table 1. For the first component, the central velocity of ^{13}CO transitions shifts from 6.51 km s^{-1} of position P1 to 5.38 km s^{-1} of P10 and then reaches 5.95 km s^{-1} of position P17. A significant second component of CO(1-0) and CO(2-1) spectra arises from $\sim 7.7 \text{ km s}^{-1}$ of P14 to $\sim 8.6 \text{ km s}^{-1}$ of P17. In this study, we focus on the physical properties of the first velocity component. Discussion about the second velocity component is in Section 4.

Goldsmith et al. (2016) confirmed similar velocity gradient in the boundary of L1599B and treated this as the rotation of the central portion of the cloud about its long axis. However, the velocity gradient in this linear edge is not monotonic, implying a low possibility of the cloud rotation. This velocity gradient is also seen in both OH and CH spectra and is interpreted as the effect of C-shock (Xu et al. 2016; Xu & Li 2016).

The integrated intensity of multi-J transitions of CO and ^{13}CO toward the first velocity component is presented in Fig. 4. The intensity values of CO(1-0) and CO(2-1) reaches maximum at P9, the position outside linear edge. The intensity of other three lines reaches maximum value toward P12, the position inside linear edge.

3.2. Ratios of Integrated Intensity

We first inspect the intensity ratio of ^{12}CO and ^{13}CO in the J=1-0 transition, R_{1-0} and the intensity ratio of ^{12}CO and ^{13}CO in the J=2-1 transition, R_{2-1} toward the first velocity component. These two ratios are affected by both the $^{12}\text{C}/^{13}\text{C}$ value and optical depth. As shown in Fig. 5, R_{1-0} does not exceed 20 while R_{2-1} reaches a maximum of 54 outside the linear edge. This discrepancy stems from the non-negligible opacity of CO(1-0). With the assumption of optically thin and same excitation temperature of CO and ^{13}CO , the R_{2-1} value toward P3 provides an isotopic $^{12}\text{C}/^{13}\text{C}$ ratio of 54 ± 17 in this region. This value represents a lower limit considering opacity effects.

Our finding of the isotopic $^{12}\text{C}/^{13}\text{C}$ ratio is consistent with the indicated low ambient value of 43 across this edge (Orr et al. 2014) and the value of 59 – 76 in local ISM (Lucas & Liszt 1998; Wilson 1999; Milam et al. 2005; Sheffer et al. 2007; Stahl et al. 2008; Ritchey et al. 2011). However, this isotopic value is much lower than that of ~ 90 based on ^{13}CO isotopologs of HCCNC and

HNCCC observations toward TMC-1 (Cernicharo et al. 2024).

Intensity ratio of CO(2-1)/CO(1-0) (hereafter, R_{21}^{12}) and $^{13}\text{CO}(2-1)/^{13}\text{CO}(1-0)$ (hereafter, R_{21}^{13}) are sensitive to kinetic temperature and volume density. As shown in Fig. 6, R_{21}^{12} value varies from 0.48 to 0.82 with a median value of 0.70. The R_{21}^{13} value is systematically lower. It varies from 0.13 to 0.56 with median value of 0.48.

For optically thick transitions, excitation temperature T_{ex} is related with main beam brightness temperature T_{mb} through (e.g., Penzias 1975; Garden et al. 1991; Goldsmith et al. 2016),

$$T_{\text{ex}} = \frac{h\nu/k}{\ln\left(1 + \frac{h\nu/k}{T_{\text{mb}} + B}\right)}, \quad (1)$$

where h, k , and ν are Planck constant, Boltzmann constant and frequency of the transition. $B = \frac{h\nu/k}{e^{h\nu/(kT_{\text{bg}})} - 1}$, where T_{bg} is taken as the cosmic microwave background of 2.73 K. Derived T_{ex} value for multi-J transitions of CO is shown in Table 2. The T_{ex} value varies from ~ 5 K toward outermost position to maximum value of ~ 10 K.

Since $^{13}\text{CO}(2-1)$ and $^{13}\text{CO}(1-0)$ transitions are optically thin, their intensity ratio R_{21}^{13} and the excitation temperature of $J=2-1$, $T_{\text{ex}}(2-1)$ are connected by the equation $R_{21}^{13} = \frac{\int T_{\text{mb}}(2-1)dv}{\int T_{\text{mb}}(1-0)dv} = 4e^{-10.6/T_{\text{ex}}(2-1)}$ (Goldsmith et al. 1975). However, this equation adopts *Rayleigh – Jeans* approximation and ignores the 2.73 K cosmic microwave background. It will underestimate R_{21}^{13} by 20% for $T_{\text{ex}}(2-1) = 5$ K and 2% for $T_{\text{ex}}(2-1) = 20$ K (Loren et al. 1981). Under optically thin and LTE assumption, we derive an accurate relationship based on equations in Mangum & Shirley (2015),

$$\begin{aligned} R_{21}^{13} &= \frac{\int T_{\text{mb}}(2-1)dv}{\int T_{\text{mb}}(1-0)dv} = f \frac{A_{21}g_2\nu_{10}^2}{A_{10}g_1\nu_{21}^2} e^{-\Delta E_{21}/(kT_{\text{ex}}(2-1))} \\ &= f \cdot 4e^{-10.6/T_{\text{ex}}(2-1)}, \end{aligned} \quad (2)$$

in which A_{ul} and ν_{ul} represent the spontaneous emission coefficient and rest frequency for the transition $u \rightarrow l$ of ^{13}CO . $g_u = 2J_u + 1$ is rotational degeneracy of the upper energy level. The correction factor f is expressed with

$$f = \frac{J_{\nu_{10}}(T_{\text{ex}}(2-1)) J_{\nu_{21}}(T_{\text{ex}}(2-1)) - J_{\nu_{21}}(T_{\text{bg}})}{J_{\nu_{21}}(T_{\text{ex}}(2-1)) J_{\nu_{10}}(T_{\text{ex}}(2-1)) - J_{\nu_{10}}(T_{\text{bg}})}, \quad (3)$$

in which *Rayleigh–Jeans equivalent temperature*, $J_{\nu}(T) = \frac{h\nu/k}{\exp(h\nu/kT) - 1}$. The f value approaches 1

when *Rayleigh – Jeans* approximation $\frac{h\nu}{kT_{\text{ex}}} \ll 1$ and $T_{\text{bg}} \ll T_{\text{ex}}$ are satisfied.

The $T_{\text{ex}}(2-1)$ value of these 20 positions ranges from 2.80 to 4.82 K (see Table 2). The derived value is significantly lower than typical kinetic temperature of 10 K in diffuse molecular regions (Goldsmith et al. 2008), indicating the necessity of non-LTE calculations for ^{13}CO .

3.3. Modeling Multi-transitions of CO with RADEX

In order to accurately calculate physical parameters including kinetic temperature, density, and CO column density $N(\text{CO})$, we adopt the RADEX code (van der Tak et al. 2007), which is efficient in deriving physical parameters of clouds under non-LTE and uniform conditions. Markov Chain Monte Carlo (MCMC) method (Foreman-Mackey et al. 2013) is adopted to find optimum solutions to maximize the likelihood function. To minimize the effect of beam filling factor, we use intensity ratios of 4 transition lines including CO(2-1), CO(3-2), $^{13}\text{CO}(1-0)$ and $^{13}\text{CO}(2-1)$ with respect to CO(1-0) as input parameters. Since no $^{13}\text{CO}(2-1)$ emission is detected toward EP3, EP2, EP1 and P5, we only use intensity ratios of the remaining 3 transition lines as input. The likelihood function is defined with

$$\ln p = -\frac{1}{2} \sum_k \left[\frac{(R_{\text{obs}}^k - R_{\text{model}}^k)^2}{\sigma_{\text{obs}}^k{}^2} + \ln(2\pi\sigma_{\text{obs}}^k{}^2) \right], \quad (4)$$

where the R_{obs}^k and σ_{obs}^k are the k th intensity ratio and its uncertainty, respectively. R_{model}^k is the modeled intensity ratio from RADEX.

A lower value of $^{12}\text{C}/^{13}\text{C} = 54 \pm 17$ is derived in Section 3.2. We adopted a fixed $^{12}\text{C}/^{13}\text{C}$ ratio of 54 in RADEX calculations, resulting in $N(\text{CO})/N(^{13}\text{CO})=54$. This would decrease the freedom of parameters and benefit obtaining better constraints with MCMC fit.

With the large velocity gradient approximation (LVG; Sobolev 1957), RADEX calculations cover the following range of physical parameters: $5\text{K} \leq T_k \leq 10^3\text{K}$, $1\text{cm}^{-3} \leq n_{\text{H}_2} \leq 10^4\text{cm}^{-3}$, and $10^{13}\text{cm}^{-2} \leq N_{^{13}\text{CO}} \leq 10^{18}\text{cm}^{-2}$. The input line width for RADEX plays a critical role in the modeling process. We utilized the observed line width of $^{13}\text{CO}(1-0)$, a transition known to be optically thin. As an example, MCMC fitting toward P6 is shown in Fig. 7. The value and its uncertainty of each physical parameter are derived by adopting 50 and [16, 84] percentile of MCMC samples. Derived physical parameters toward 20 positions are shown in Table 2 and Fig. 8.

The MCMC fits converge for three physical parameters toward all 20 positions. The T_k value ranges from 8.71 to 436 K. It decreases from EP3 to P2 and then

increases to a peak value of ~ 28.84 K toward P5. The n_{H_2} value varies from 26.9 to $2.0 \times 10^3 \text{ cm}^{-3}$. An obvious jump of n_{H_2} value is found from P6 to P7, corresponding to the position with peak H_2 intensity. The $N(^{13}\text{CO})$ value spans from 1.20×10^{14} to $3.02 \times 10^{15} \text{ cm}^{-2}$.

A uniform density was adopted in RADEX calculations. However, the clumpy structure of the molecular gas (e.g., [Hennebelle et al. 2008](#); [Zucker et al. 2020](#)) will make the uniform assumption invalid. With CH observations, [Xu & Li \(2016\)](#) found the presence of C-shock in this region, which is not included in the modeling calculations yet. All of the above discrepancy will introduce uncertainties into our results.

Table 1. Gaussian fitting parameters of CO data.

Pos	CO(1-0)				CO(2-1)				CO(3-2)					
	T_{peak} K	V_{cen} km s ⁻¹	ΔV km s ⁻¹	ΔV km s ⁻¹	T_{peak} K	V_{cen} km s ⁻¹	ΔV km s ⁻¹	ΔV km s ⁻¹	T_{peak} K	V_{cen} km s ⁻¹	ΔV km s ⁻¹	ΔV km s ⁻¹		
EP3	2.12(2)	6.42(1)	1.08(1)	1.51(6)	1.22(3)	6.39(1)	0.90(1)	—	—	—	—	0.40(12)	6.59(15)	1.01(15)
EP2	3.25(3)	6.51(0)	0.98(0)	1.28(4)	1.90(3)	6.50(1)	0.88(1)	—	—	—	—	0.82(14)	6.56(5)	0.62(5)
EP1	3.64(4)	6.61(0)	0.97(1)	1.07(3)	2.14(3)	6.61(1)	0.90(1)	—	—	—	—	0.97(7)	6.65(2)	0.67(3)
P1	3.49(4)	6.70(1)	1.14(1)	1.12(2)	2.04(3)	6.73(1)	1.07(1)	—	—	—	—	0.85(17)	6.83(5)	0.52(5)
P2	2.95(3)	6.70(1)	1.32(1)	1.24(2)	1.79(3)	6.76(1)	1.23(1)	—	—	—	—	0.53(9)	6.73(5)	0.62(5)
P3	2.79(3)	6.72(1)	1.40(1)	1.29(2)	1.82(3)	6.77(1)	1.28(1)	—	—	—	—	0.42(5)	6.71(9)	1.44(9)
P4	2.58(8)	6.61(2)	1.31(2)	0.90(4)	1.75(4)	6.71(1)	1.35(1)	—	—	—	—	0.75(6)	6.73(4)	0.97(4)
P5	2.45(9)	6.54(3)	1.54(3)	0.69(4)	1.71(4)	6.63(2)	1.55(2)	—	—	—	—	0.67(5)	6.65(5)	1.25(5)
P6	2.50(9)	6.37(3)	1.87(3)	0.74(3)	1.79(4)	6.48(2)	1.95(2)	—	—	—	—	0.87(6)	6.63(4)	1.31(4)
P7	3.39(7)	6.26(2)	2.08(2)	0.90(2)	2.30(4)	6.35(2)	2.18(2)	—	—	—	—	1.39(6)	6.51(3)	1.33(3)
P8	3.24(7)	6.01(3)	2.60(3)	0.85(3)	2.25(4)	6.12(2)	2.55(2)	—	—	—	—	1.10(5)	6.07(5)	2.20(5)
P9	3.87(10)	5.78(3)	2.54(4)	1.76(4)	2.74(5)	5.89(2)	2.52(2)	—	—	—	—	1.58(5)	5.72(3)	2.12(3)
P10	4.47(16)	5.66(4)	2.48(5)	1.12(2)	3.21(7)	5.76(3)	2.45(3)	—	—	—	—	2.24(4)	5.68(2)	1.90(2)
P11	4.85(22)	5.62(6)	2.63(6)	1.30(2)	3.71(11)	5.64(4)	2.46(4)	—	—	—	—	3.06(5)	5.56(1)	1.73(1)
P12	4.56(19)	5.93(5)	2.67(6)	0.96(1)	3.77(11)	5.88(3)	2.45(4)	—	—	—	—	3.37(4)	5.67(1)	1.59(1)
P13	4.55(17)	6.15(4)	2.34(4)	0.86(1)	3.56(9)	6.14(3)	2.30(3)	—	—	—	—	3.31(4)	5.86(1)	1.33(1)
P14	5.92(31)	5.74(5)	1.60(3)	0.84(0)	4.49(27)	5.79(2)	1.66(3)	—	—	—	—	3.75(8)	5.86(1)	1.22(1)
P14	1.46(14)	7.70(29)	2.35(22)	—	0.90(8)	7.71(39)	3.12(26)	—	—	—	—	—	—	—
P15	5.67(36)	5.67(4)	1.75(4)	0.80(1)	4.39(17)	5.75(2)	1.72(2)	—	—	—	—	3.99(9)	5.89(1)	1.13(1)
P15	1.24(12)	7.92(41)	3.12(32)	—	0.85(6)	7.92(28)	3.09(21)	—	—	—	—	—	—	—
P16	5.54(13)	5.68(3)	1.94(3)	0.67(1)	4.20(5)	5.77(2)	1.93(1)	—	—	—	—	3.21(9)	5.84(2)	1.38(2)
P16	1.22(12)	8.54(14)	2.21(15)	—	0.80(5)	8.57(9)	2.28(9)	—	—	—	—	—	—	—
P17	5.83(12)	5.80(2)	1.73(2)	0.79(1)	4.58(6)	5.92(1)	1.81(1)	—	—	—	—	3.17(8)	5.89(2)	1.31(2)
P17	1.21(11)	8.61(10)	2.05(11)	—	0.86(6)	8.76(7)	1.83(7)	—	—	—	—	—	—	—

3.4. HINSA Column Density and Abundance

As seen in Fig. 3, an obvious HINSA feature with a central velocity of ~ 6 km s $^{-1}$ can be found from P4 to P17. We follow the HINSA analysis in (Li & Goldsmith 2003) and (Tang et al. 2020). The observed HI brightness temperature can be derived through

$$T_{ab}(v) = [pT_{HI}(v) + (T_c - T_{ex})(1 - \tau_f)](1 - e^{-\tau}), \quad (5)$$

where T_c and T_x are the background continuum temperature and the excitation temperature, respectively. The value for T_c is derived from the CHIPASS continuum survey at 1.4 GHz (Calabretta et al. 2014). T_x is assumed to be equal to T_K , which is reasonable for HI in the center of molecular clouds, where non-thermal processes are weak (Shaw et al. 2017). The term τ_f represents the optical depth of the foreground HI gas. The parameter p is defined as the fraction of τ_f relative to the total HI optical depth along the line of sight. Given the Taurus cloud's high Galactic latitude, the parameter p can be estimated using the vertical HI distribution of the Milky Way. We adopt the formula for p from Li & Goldsmith (2003):

$$p = \operatorname{erfc} \left[\frac{\sqrt{4 \ln(2)} D \sin(|b|)}{z} \right], \quad (6)$$

where D is the distance to the Taurus cloud, b is the Galactic latitude, z is the FWHM vertical extent of the Galactic HI disk and $\operatorname{erfc}(x)$ is the complementary error function, defined as:

$$\operatorname{erfc}(x) = 1 - (2/\pi^{1/2}) \int_0^x e^{-t^2} dt. \quad (7)$$

For $b = -13.0$, the value of p decreases from 0.88 to 0.79 as D varies from 100 pc to 180 pc. In this study, we adopt $p = 0.83$, corresponding to $D = 140$ pc (Palmeirim et al. 2013). Due to the difficulty in determining an accurate value for τ_f , we assume $\tau_f = 0.1$, which may introduce an uncertainty of approximately 4% in the typical T_{HI} value (Li & Goldsmith 2003). The same values of p and τ_f are applied to all positions, ensuring that they do not affect the relative HINSA column density across the linear edge. Fig. 9 shows the example of HINSA fitting toward P6.

After determining optical depth τ , excitation temperature T_{ex} and FWHM of the HINSA emission ΔV , HINSA column density is calculated using the following equation (Li & Goldsmith 2003):

$$N(\text{HINSA}) = 1.9 \times 10^{18} \tau T_{ex} \Delta V \text{ cm}^{-2}. \quad (8)$$

The T_k values are adopted from Table 2. The derived HINSA column density of 14 positions is presented in

Table 2. The HINSA column density, $N(\text{HINSA})$, ranges from $(5.17 \pm 4.32) \times 10^{18}$ cm $^{-2}$ at P4 to $(2.65 \pm 1.18) \times 10^{19}$ cm $^{-2}$ at P5. Kinetic temperature significantly influences the calculation of $N(\text{HINSA})$. For instance, a kinetic temperature value of 29 K yields $N(\text{HINSA})$ of 2.7×10^{19} cm $^{-2}$ at P5, whereas this value decreases to 3.6×10^{18} cm $^{-2}$ if $T_k = 10$ K at the same position.

The total column density, N_H , is determined from the $E(B-V)$ value with $N_H/E(B-V) = 9.4 \times 10^{21}$ cm $^{-2}$ mag $^{-1}$ (Nguyen et al. 2018), not the canonical value of $5.8 \times 10^{21} E(B-V)$ cm $^{-2}$ mag $^{-1}$ (Bohlin et al. 1978), but one favored by recent studies (Lenz et al. 2017; Fitzpatrick et al. 2019). The HINSA abundance is calculated as $x = N(\text{HINSA})/N_H$. As shown in Fig. 10, the HINSA abundance has a peak at 5.9×10^{-3} toward P5 and minimum value of 7.0×10^{-4} toward P16. These values are consistent with the value in the Taurus region, for instance, 2.5×10^{-4} toward the L1544 cloud and $\sim 2 \times 10^{-3}$ toward the L1574 cloud (Li & Goldsmith 2003).

4. DISCUSSION

4.1. Formation of Cold Dense Flow by Shock Compression

Many numerical simulations have investigated the transition from HI to H $_2$ gas under various environments (e.g., Glover et al. 2010; Vázquez-Semadeni et al. 2010; Clark et al. 2012; Valdivia et al. 2016; Seifried et al. 2022). In these simulations, the presence of shocks is considered to accelerate this process (e.g., Koyama & Inutsuka 2002; Mac Low et al. 2005). Follow up simulations in realistic environment, e.g., collision of gas streams at moderately supersonic velocities (Vázquez-Semadeni et al. 2006, 2007) and collision of superbubbles (Ntormousi et al. 2011) found the formation of cold, dense, and filamentary structure in the collision zone.

Li et al. (2015) identified 37 bubbles in the Taurus molecular cloud, suggesting the presence of shocks in this region. According to simulations, the presence of shocks can result in a sharp density increase of H $_2$ across the shock front (e.g., Chieze et al. 1998). As shown in Section 3, an apparent jump of H $_2$ density and the appearance of cold HI gas mixed with molecular gas are observed from the outer region into the inner region. Our observations are consistent with simulations of shock-accelerated H $_2$ formation. However, further observations of shock tracers (e.g., SiO ($J = 2 - 1$)) across the linear edge are essential to validate the proposed shock-induced H $_2$ formation.

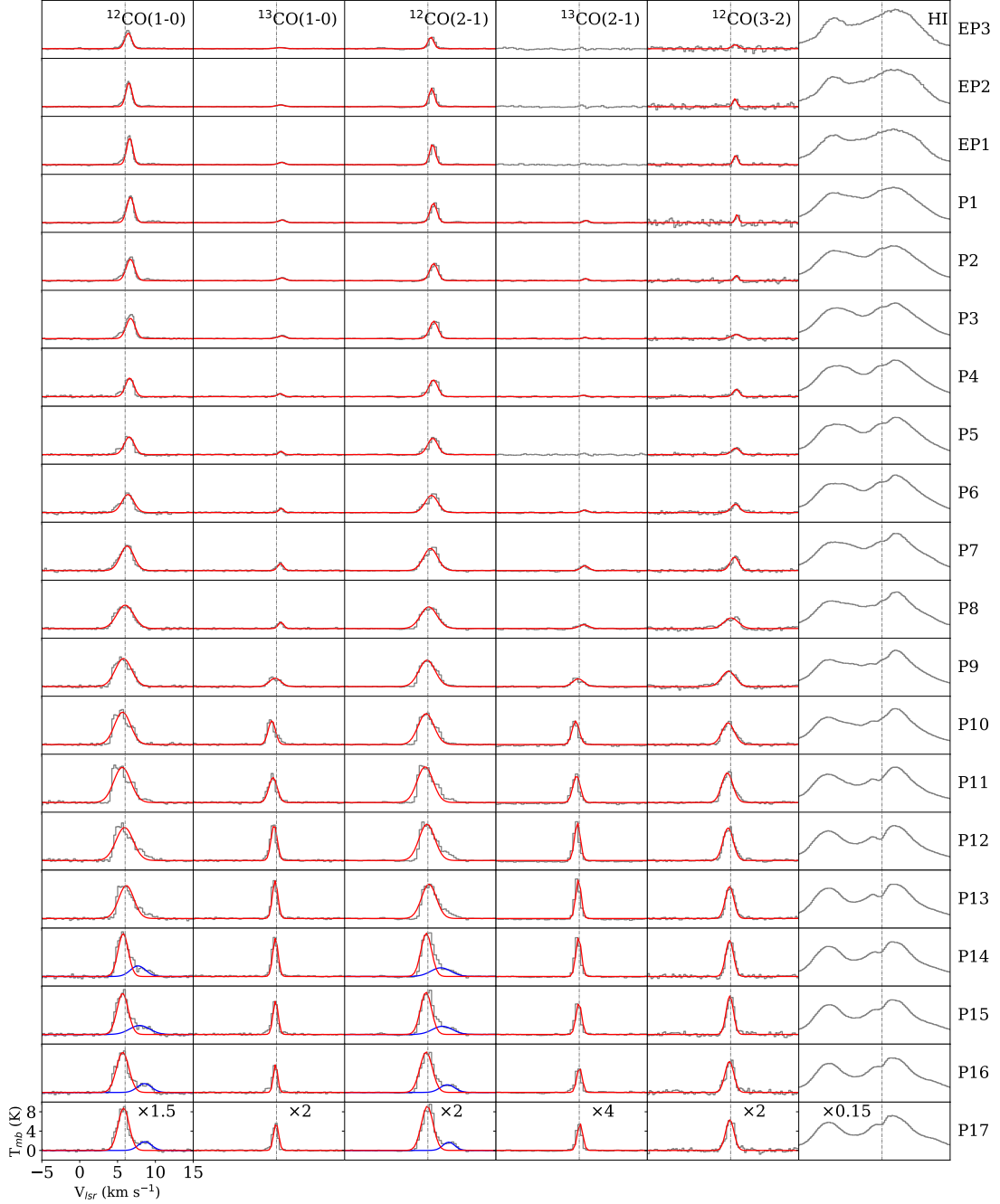


Figure 3. Spectra of CO/¹³CO(1-0), CO/¹³CO(2-1), CO(3-2) and HI of the first velocity component across the linear edge. All the spectra were convolved to 3' at each position. The first velocity component of CO is plotted with red Gaussian profile while the second is plotted with blue Gaussian profile. The vertical dash-dot line represent the position of 6 km s⁻¹.

Table 2. Derived physical parameters of the first velocity component. The parameter $T_{\text{ex}}^{\text{CO}(1-0)}$, $T_{\text{ex}}^{\text{CO}(2-1)}$, and $T_{\text{ex}}^{\text{CO}(3-2)}$ represent excitation temperature derived from the optically thick transitions of CO. $T_{\text{ex}}(2-1)$ represents excitation temperature of $J = 2-1$ from optically thin transitions of ^{13}CO . T_{k} , n_{H_2} , $N(^{13}\text{CO})$ and $N(\text{HINSA})$ represent fitted kinetic temperature, volume density of H_2 , column density of ^{13}CO and column density of HINSA, respectively.

Pos	E(B-V)	$T_{\text{ex}}^{\text{CO}(1-0)}$	$T_{\text{ex}}^{\text{CO}(2-1)}$	$T_{\text{ex}}^{\text{CO}(3-2)}$	$T_{\text{ex}}(2-1)$	T_{k}	$\log(\frac{n_{\text{H}_2}}{\text{cm}^{-3}})$	$\log(\frac{N(^{13}\text{CO})}{\text{cm}^{-2}})$	$N(\text{HINSA})$
	(mag)	(K)	(K)	(K)	(K)	(K)			(10^{18}cm^{-2})
EP3	0.33	5.25 (3)	5.09 (5)	4.54 (34)	—	437^{+358}_{-311}	$1.63^{+0.280}_{-0.470}$	$14.1^{+0.2}_{-0.2}$	—
EP2	0.40	6.47 (3)	6.02 (4)	5.51 (28)	—	$117^{+33.9}_{-34.3}$	$1.52^{+0.030}_{-0.110}$	$14.7^{+0.100}_{-0.100}$	—
EP1	0.38	6.88 (4)	6.33 (3)	5.81 (14)	—	$34.7^{+10.0}_{-3.77}$	$1.72^{+0.080}_{-0.050}$	$15.0^{+0.030}_{-0.020}$	—
P1	0.35	6.72 (4)	6.20 (4)	5.58 (34)	3.65 (27)	$20.4^{+0.960}_{-0.460}$	$1.91^{+0.120}_{-0.050}$	$15.0^{+0.040}_{-0.090}$	—
P2	0.42	6.15 (3)	5.88 (4)	4.86 (22)	3.31 (24)	$10.5^{+0.490}_{-0.470}$	$2.04^{+0.380}_{-0.280}$	$15.1^{+0.230}_{-0.350}$	—
P3	0.44	5.97 (3)	5.92 (5)	4.59 (14)	2.80 (26)	$8.71^{+18.8}_{-0.390}$	$1.43^{+0.080}_{-0.330}$	$15.9^{+0.740}_{-0.110}$	—
P4	0.49	5.75 (9)	5.83 (5)	5.36 (13)	3.24 (36)	$20.4^{+10.5}_{-4.20}$	$1.52^{+0.550}_{-0.300}$	$15.5^{+0.330}_{-0.660}$	5.17 ± 4.32
P5	0.39	5.61 (10)	5.77 (6)	5.18 (11)	—	$28.8^{+20.1}_{-9.79}$	$1.41^{+0.67}_{-0.97}$	$15.3^{+0.540}_{-0.800}$	26.5 ± 11.8
P6	0.31	5.66 (10)	5.88 (6)	5.60 (12)	4.03 (35)	$25.7^{+9.78}_{-5.75}$	$1.69^{+0.630}_{-0.470}$	$15.3^{+0.290}_{-0.710}$	11.5 ± 6.87
P7	0.46	6.62 (8)	6.54 (5)	6.54 (9)	4.32 (21)	$13.2^{+1.95}_{-1.96}$	$2.93^{+0.220}_{-0.200}$	$14.9^{+0.110}_{-0.120}$	6.49 ± 3.00
P8	0.53	6.46 (7)	6.47 (5)	6.05 (9)	4.80 (30)	$22.4^{+10.7}_{-6.17}$	$2.66^{+0.320}_{-0.300}$	$14.8^{+0.120}_{-0.140}$	17.7 ± 7.18
P9	0.67	7.12 (11)	7.09 (6)	6.86 (8)	4.29 (15)	$10.0^{+1.75}_{-0.880}$	$3.25^{+0.230}_{-0.200}$	$15.2^{+0.130}_{-0.090}$	11.6 ± 3.69
P10	0.74	7.75 (17)	7.65 (9)	7.85 (6)	4.49 (11)	$9.12^{+0.650}_{-0.410}$	$3.21^{+0.120}_{-0.130}$	$15.3^{+0.080}_{-0.070}$	9.57 ± 3.40
P11	0.98	8.14 (23)	8.24 (13)	8.97 (6)	4.45 (8)	$10.0^{+0.720}_{-0.670}$	$3.08^{+0.190}_{-0.140}$	$15.5^{+0.080}_{-0.130}$	10.9 ± 3.75
P12	0.99	7.84 (19)	8.30 (12)	9.37 (6)	4.55 (6)	$10.0^{+0.720}_{-0.450}$	$3.12^{+0.140}_{-0.110}$	$15.4^{+0.070}_{-0.080}$	13.1 ± 4.56
P13	0.99	7.83 (18)	8.06 (10)	9.30 (6)	4.60 (5)	$9.12^{+0.430}_{-0.410}$	$3.23^{+0.120}_{-0.100}$	$15.3^{+0.060}_{-0.070}$	8.89 ± 3.60
P14	0.88	9.25 (32)	9.12 (30)	9.87 (10)	4.71 (4)	$10.5^{+1.28}_{-0.470}$	$3.06^{+0.280}_{-0.190}$	$15.5^{+0.130}_{-0.160}$	7.72 ± 3.76
P15	0.88	8.99 (37)	9.01 (20)	10.2 (1)	4.67 (7)	$10.5^{+1.28}_{-0.920}$	$3.09^{+0.680}_{-0.220}$	$15.3^{+0.130}_{-0.520}$	6.92 ± 3.63
P16	0.79	8.87 (13)	8.80 (6)	9.18 (12)	4.82 (10)	$10.5^{+0.750}_{-0.470}$	$3.30^{+0.090}_{-0.090}$	$14.9^{+0.040}_{-0.060}$	5.80 ± 3.78
P17	0.78	9.16 (12)	9.23 (7)	9.12 (11)	4.75 (8)	$10.5^{+0.490}_{-0.240}$	$3.20^{+0.070}_{-0.070}$	$15.1^{+0.040}_{-0.050}$	7.03 ± 3.82

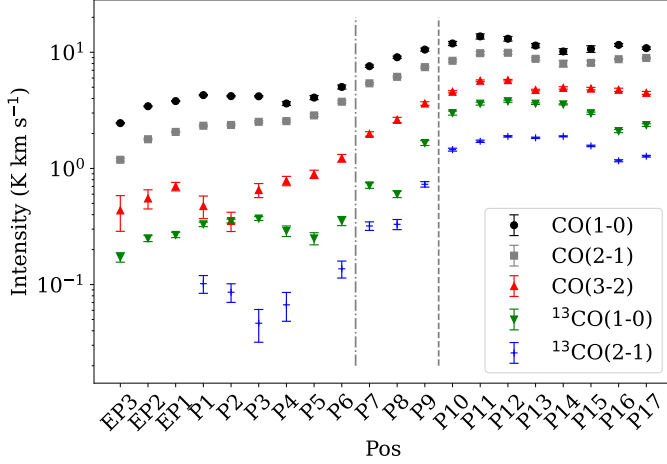


Figure 4. Integrated intensity of CO/¹³CO(1-0), CO/¹³CO(2-1), CO(3-2) of the first velocity component across Taurus linear edge. The vertical dash-dotted and dashed lines represent the spatial locations of the H₂ peak and CO edge shown in Fig. 1.

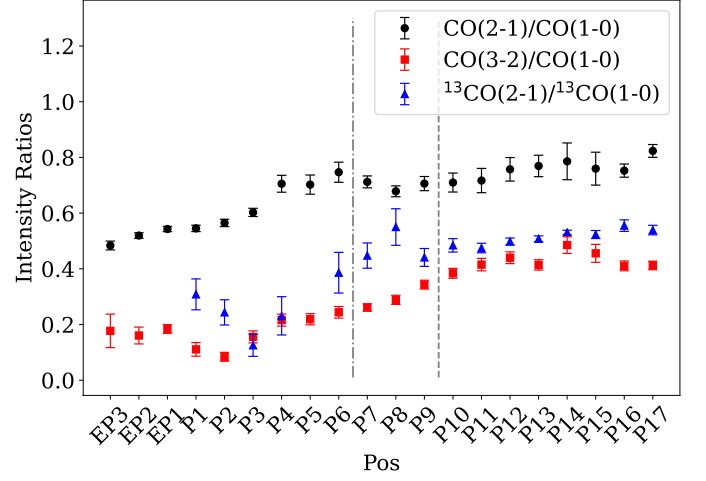


Figure 6. The intensity ratio between CO(2-1) and CO(1-0) of the first velocity component across Taurus linear edge. The vertical dash-dotted and dashed lines represent the spatial locations of the H₂ peak and CO edge shown in Fig. 1.

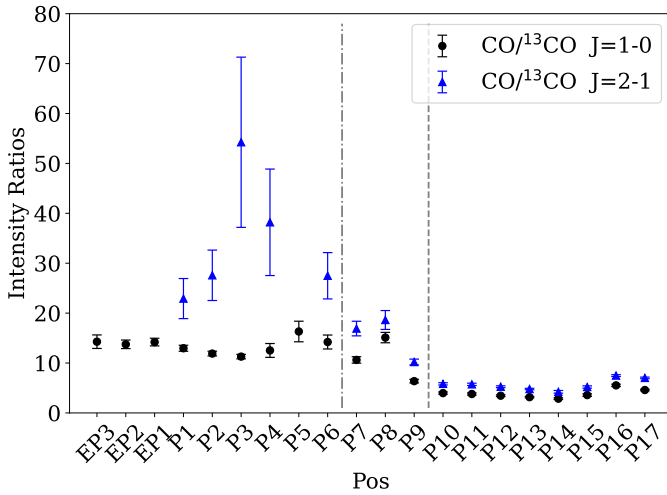


Figure 5. Intensity ratio between CO and ¹³CO in J=1-0 and J=2-1 transitions of the first velocity component across Taurus linear edge. The vertical dash-dotted and dashed lines represent the spatial locations of the H₂ peak and CO edge shown in Fig. 1.

4.2. The Relationship between Kinetic Temperature and Excitation Temperature

With UV absorptions of CO toward stars, the excitation temperature T_{ex} of low- J rotational lines of CO has been determined to be less than 5 K in diffuse molecular clouds (Sheffer et al. 2008). These findings can be explained by assuming T_{k} values of 50 or 100 K (Goldsmith 2013). The notable disparity between T_{ex} and T_{k} suggests subthermal excitation, indicating a departure from LTE conditions.

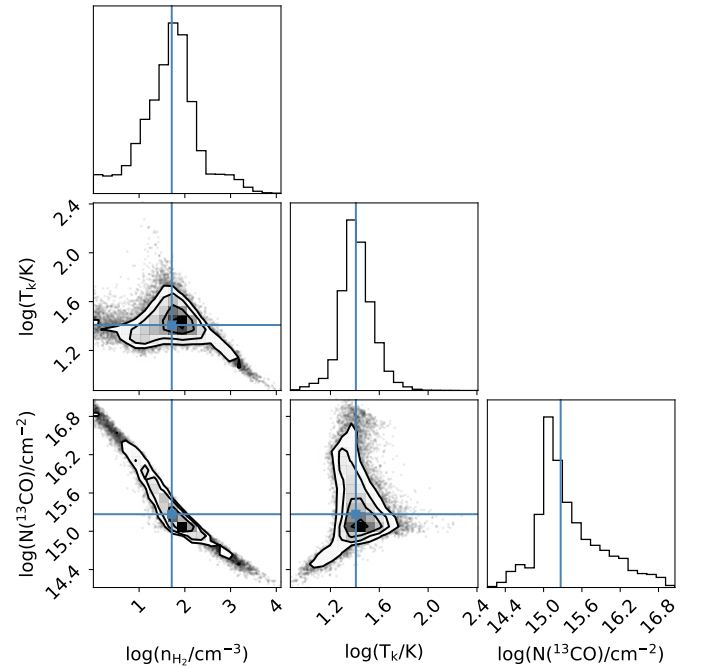


Figure 7. Parameter space of MCMC fitting toward P6 under LVG approximation.

As outlined in Table 2, the T_{ex} values rise from approximately 5 K to around ~ 10 K for multi-transitions of CO. However, the T_{ex} values derived from optically thin ¹³CO transitions are notably lower, ranging from 2.80 to 4.82 K. While both sets of calculations yield lower excitation temperature than the T_{k} values of 10 – 39 K obtained from the MCMC fit, the discrepancy for optically thick lines (low- J transitions of CO) is less pro-

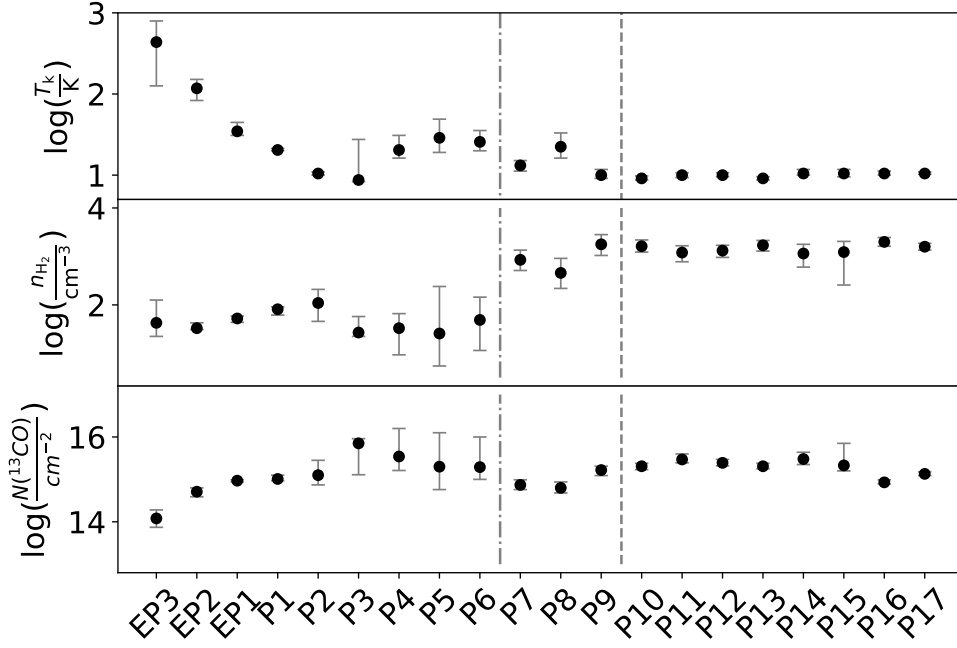


Figure 8. Derived value for physical parameters with MCMC. *Top* : Kinetic temperature, T_K ; *Middle* : Volume density of H_2 , n_{H_2} ; *Bottom* : Column density of ^{13}CO , $N(^{13}CO)$. The vertical dash-dotted and dashed lines represent the spatial locations of the H_2 peak and CO edge shown in Fig. 1.

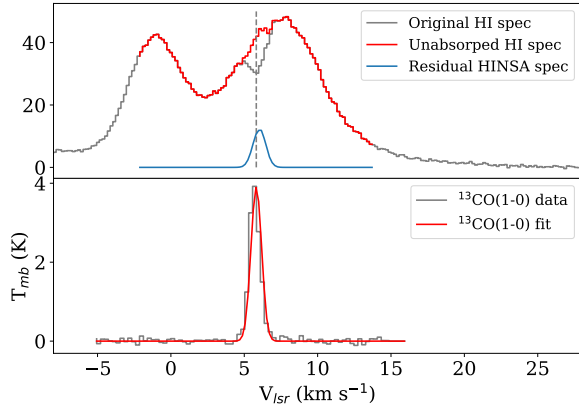


Figure 9. HINSA fitting of HI spectrum toward P13.

nounced. Calculation of physical parameters under LTE conditions are likely to introduce less uncertainty for optically thick lines.

4.3. Cloud Geometry Revealed by Multi- J CO Transitions

With observations of CO, [C I], and [C II], Goldsmith et al. (2010) and Orr et al. (2014) proposed a cylindrical geometry to model this linear edge region with a two-dimensional RATRAN radiative transfer code. The fitted volume density follows a power law with the distance

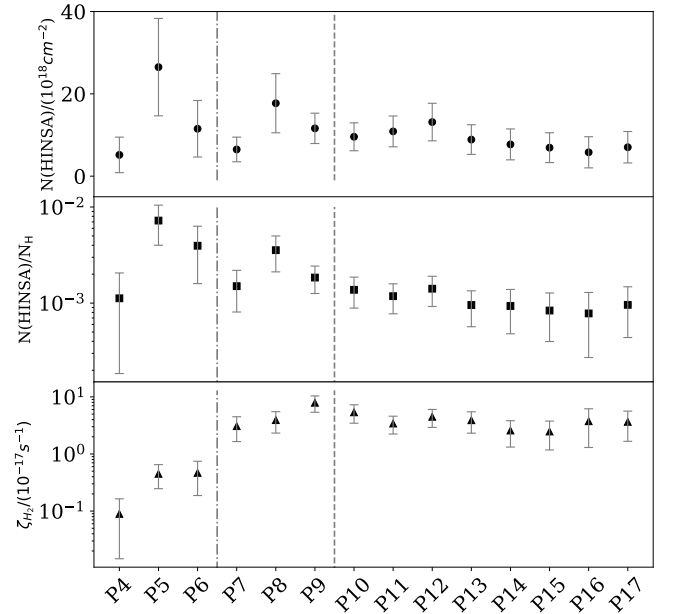


Figure 10. HINSA column density $N(\text{HINSA})$ (top panel), HINSA abundance (middle panel) and ζ_{H_2} (lower panel) toward P4 to P17. The vertical dash-dotted and dashed lines represent the spatial locations of the H_2 peak and CO edge shown in Fig. 1.

to the core within a truncating radius, that is described by:

$$n_{H_2}(r) = \begin{cases} n_c a^2 / (r^2 + a^2) & , r \leq R \\ 0 & , r > R \end{cases}, \quad (9)$$

where n_{H_2} is the volume density of H₂, r is the distance to the center of the cylindrical, n_c is the maximum volume density corresponding to the center of the cylindrical, a is the width of the central core, and R is the truncating radius. The value of n_c , a and R are 626 cm⁻³, 0.457 pc, and 1.80 pc, respectively. With this model, the peak H₂ volume density towards 20 sight-lines ranges from 50 to 620 cm⁻³ (Fig. 11) except EP3, whose position exceeds the radius in Orr et al. (2014).

As shown in Fig. 11, the volume densities derived using the one-dimensional RADEX code in this study are significantly higher than the peak volume densities in the model of Orr et al. (2014), except for positions P3 to P6. However, we note that our analysis incorporates higher- J transitions of ¹²CO and ¹³CO (up to $J=3-2$), while excluding [C I] and [C II] lines, which primarily trace the diffuse gas component. This methodological difference likely explains the higher volume densities derived in our model than that in Orr et al. (2014).

Beside the inconsistency of volume density, the cylindrical geometry can not explain the velocity difference of 1–3 km s⁻¹ between two velocity components, which is clearly seen in CO(1-0) and CO(2-1) data. The presence of two velocity components is observed in OH emission too (Xu et al. 2016). There exists a U shape around the linear edge (see details of Fig. 1), which is consistent with the prediction of numerical cloud-cloud simulation (e.g., Navarrete et al. 2024). The consistency suggests that this linear edge may be due to the collision of a massive gas stream (the first velocity component centering 5.6–6.7 km s⁻¹) and a gas stream with a much lower H₂ column density (the second velocity component centering 7.7–8.6 km s⁻¹).

4.4. Low-energy Cosmic Ray Ionization Rate across the Linear edge

The cold HI responsible for the HINSA feature originates from the dissociation of H₂ by low-energy cosmic rays. When the dissociation of H₂ reaches equilibrium with the formation of H₂ on dust grains, the abundance of cold HI remains constant over time, indicating a steady-state condition. Under this condition, the low-energy cosmic ray ionization rate of H₂ ζ_{H_2} can be expressed with the formulation in Goldsmith & Li (2005),

$$\zeta_{H_2} = \frac{2k'n_0x}{1-x}, \quad (10)$$

where k' , n_0 and x represent the formation rate coefficient of H₂, the total volume density, and the HI

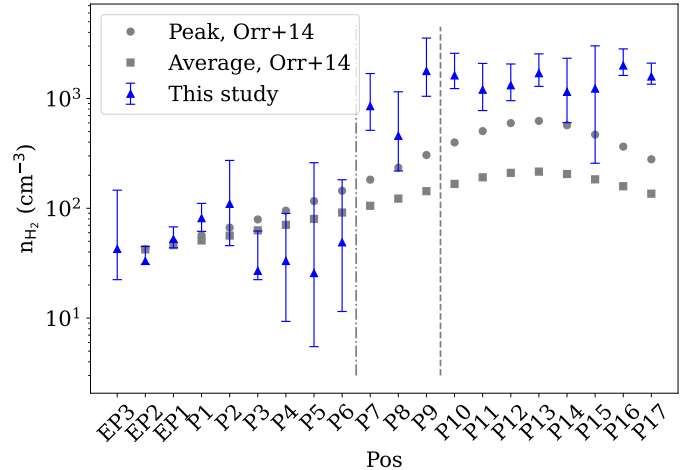


Figure 11. Volume density of H₂, n_{H_2} towards 20 positions. Peak and average density along line of sight are marked with black dots and blue triangles, respectively. The position of EP3 exceeds the radius of cylinder in Orr et al. (2014). Its density was adopted as 0 cm⁻³. The vertical dash-dotted and dashed lines represent the spatial locations of the H₂ peak and CO edge shown in Fig. 1.

abundance, respectively. The composition and size distribution of grains can strongly affect the value of k' by an order of magnitude (Habart et al. 2004; Goldsmith & Li 2005). We have adopted the general expression from Goldsmith & Li (2005), which gives $k' = 1.2 \times 10^{-17}$ cm³ s⁻¹ at $T_k = 10$ K.

As shown in Fig. 10, the value of ζ_{H_2} peaks at a maximum of $(7.9 \pm 2.5) \times 10^{-17}$ s⁻¹ toward P9. This closely aligns with the range of $(3 - 6) \times 10^{-17}$ s⁻¹ in Orr et al. (2014). However, the ionization rate experiences a two-order-of-magnitude variation, reaching approximately $(8.9 \pm 7.5) \times 10^{-19}$ s⁻¹ toward P4. This variability can be attributed to the significant changes in number density observed across the linear edge.

4.5. Influence and Physical State of the Second Velocity Component

The presence of the second velocity component is notably evident in the CO(1-0) and CO(2-1) emissions spanning from P14 to P17. Determining the physical properties of the second velocity component would significantly benefit unraveling its origin. However, this task is challenging due to the lack of observations of optically thin lines. To enhance constraints on the physical environment, we assume a beam filling factor of 1 for the second velocity component. With this assumption, we simultaneously fit the intensity of CO(1-0) and CO(2-1) by varying n_{H_2} , T_k and the ¹²CO column density $N(\text{CO})$.

The fitting results suggest that the second component has an H_2 density of $n_{\text{H}_2} \sim 1500 \text{ cm}^{-3}$, a kinetic temperature of $T_k \sim 15 \text{ K}$, and a CO column density of $N(\text{CO}) \sim 3 \times 10^{15} \text{ cm}^{-2}$. Assuming the same CO abundance of 3×10^{-5} toward P10, the H_2 column density of the second component is estimated to be approximately $1 \times 10^{20} \text{ cm}^{-2}$. These results suggest that the second component is a dense molecular cloud with a relatively low $N(\text{H}_2)$ value. Further observations are needed to better characterize its physical properties.

5. SUMMARY

We derived multiple transitions of CO and ^{13}CO data toward 20 positions across the linear edge of the Taurus molecular cloud. By combining the CO data with archival HI data, we obtained physical properties and HINSA abundance across the edge. Quantitative comparison with hydrodynamical simulations tentatively indicate that colliding gas flow shocks could drive the atomic-to-molecular phase transition along the linear edge. The main results can be summarized as follows:

1. Two velocity components with varying central velocities are identified. The main velocity component, centered at $\sim 6 \text{ km s}^{-1}$ is detected in all multi- J CO data while the second component, centered at $\sim 8 \text{ km s}^{-1}$ is observed in the CO(1-0) and CO(2-1) data within the linear edge.
2. The intensity ratio between ^{12}CO and ^{13}CO in the $J = 2 - 1$ transition implies a lower limit for the $^{12}\text{C}/^{13}\text{C}$ ratio of 54 ± 17 . This value is consistent with those found in the local ISM and with the value of 90 inferred for TMC-1 from recent HC-CNC and HNCCC observations.
3. The excitation temperature ranges from 5 to 10 K when derived from CO(1-0) data under the optically thick assumption. Assuming optically thin conditions and LTE, the excitation temperature varies from 2.80 to 4.82 K based on the intensity ratio between $^{13}\text{CO}(2-1)$ and $^{13}\text{CO}(1-0)$ data. These are significantly lower values compared to typical kinetic temperatures in molecular clouds, indicating subthermal excitation conditions.
4. We combine MCMC and non-LTE RADEX analyses to calculate the physical properties at these positions. Under a one-dimensional uniform geometry, kinetic temperature is found to range from 8.71 K to 436 K. Additionally, the number density ranges from 7.0 to $2.0 \times 10^3 \text{ cm}^{-3}$, while $N(^{13}\text{CO})$

varies from 1.20×10^{14} to $3.02 \times 10^{15} \text{ cm}^{-2}$ (Fig. 8). An obvious jump of number density appears in the position with peak H_2 intensity, which does not align with the cylindrical model proposed by Orr et al. (2014) (Fig. 11).

5. Cold HI gas appearing as HINSA feature is detected across the linear edge. Assuming a steady state, the HINSA abundance indicates a peak low-energy cosmic ray ionization rate of $\sim 6.9 \times 10^{-17} \text{ s}^{-1}$ toward P9 (Fig. 10), the position outside the $^{13}\text{CO}(1-0)$ edge.
6. The second velocity component can be characterized with physical properties of $n_{\text{H}_2} \sim 1500 \text{ cm}^{-3}$, $T_k \sim 15 \text{ K}$ and $N(\text{CO}) \sim 3 \times 10^{15} \text{ cm}^{-2}$. This component exhibits a similar number density and kinetic temperature but a smaller column density compared to the main velocity component. One possible explanation is that the linear edge could be a result of the collision between the main and the secondary velocity components.

ACKNOWLEDGMENTS

We are grateful to the anonymous referee for the constructive suggestions, which have greatly improved this paper. We appreciate Zhiyu Zhang and Jing Zhou for their valuable suggestions regarding the use of RADEX and MCMC. This work is sponsored by the National Natural Science Foundation of China (grant No. 11988101, 12473023), The University Annual Scientific Research Plan of Anhui Province (No. 2023AH030052, No. 2022AH010013), the National SKA Program of China (grant No. 2022SKA0120101), the China Manned Space Program through its Space Application System, Zhejiang Lab Open Research Project (NO. K2022PE0AB01), Cultivation Project for FAST Scientific Payoff and Research Achievement of CAMS-CAS. Di Li is a New Cornerstone Investigator and is supported by National Key R&D Program of China No. 2023YFE0110500, grant NSF PHY-2309135 to the Kavli Institute for Theoretical Physics (KITP).

The University of Arizona Submillimeter Telescope on Mt. Graham is operated by the Arizona Radio Observatory (ARO), Steward Observatory, University of Arizona. Part of CO data were observed with the Delingha 13.7 m telescope of the Qinghai Station of Purple Mountain Observatory. We appreciate all the staff members of the Delingha observatory for their help during the observations.

REFERENCES

- Biegging, J. H., Peters, W. L., & Kang, M. 2010, *ApJS*, 191, 232. doi:10.1088/0067-0049/191/2/232
- Biegging, J. H., Patel, S., Peters, W. L., et al. 2016, *ApJS*, 226, 13. doi:10.3847/0067-0049/226/1/13
- Biegging, J. H., Patel, S., Hofmann, R., et al. 2018, *ApJS*, 238, 20. doi:10.3847/1538-4365/aaade01
- Biegging, J. H., Revelle, M., & Peters, W. L. 2014, *ApJS*, 214, 7. doi:10.1088/0067-0049/214/1/7
- Bohlin, R. C., Savage, B. D., & Drake, J. F. 1978, *ApJ*, 224, 132. doi:10.1086/156357
- Calabretta, M. R., Staveley-Smith, L., & Barnes, D. G. 2014, *PASA*, 31, e007. doi:10.1017/pasa.2013.36
- Cernicharo, J., Tercero, B., Cabezas, C., et al. 2024, *A&A*, 682, L13. doi:10.1051/0004-6361/202348822
- Chieze, J.-P., Pineau des Forets, G., & Flower, D. R. 1998, *MNRAS*, 295, 672. doi:10.1046/j.1365-8711.1998.01391.x
- Clark, P. C., Glover, S. C. O., Klessen, R. S., et al. 2012, *MNRAS*, 424, 2599. doi:10.1111/j.1365-2966.2012.21259.x
- Dawson, J. R., McClure-Griffiths, N. M., Dickey, J. M., et al. 2011, *ApJ*, 741, 85. doi:10.1088/0004-637X/741/2/85
- Dawson, J. R., Ntormousi, E., Fukui, Y., et al. 2015, *ApJ*, 799, 64. doi:10.1088/0004-637X/799/1/64
- Fitzpatrick, E. L., Massa, D., Gordon, K. D., et al. 2019, *ApJ*, 886, 108. doi:10.3847/1538-4357/ab4c3a
- Foreman-Mackey, D., Hogg, D. W., Lang, D., et al. 2013, *PASP*, 125, 306. doi:10.1086/670067
- Garden, R. P., Hayashi, M., Gatley, I., et al. 1991, *ApJ*, 374, 540. doi:10.1086/170143
- Glover, S. C. O., Federrath, C., Mac Low, M.-M., et al. 2010, *MNRAS*, 404, 2. doi:10.1111/j.1365-2966.2009.15718.x
- Goldsmith, P. F., Plambeck, R. L., & Chiao, R. Y. 1975, *ApJL*, 196, L39. doi:10.1086/181739
- Goldsmith, P. F. & Li, D. 2005, *ApJ*, 622, 938. doi:10.1086/428032
- Goldsmith, P. F. 2013, *ApJ*, 774, 134. doi:10.1088/0004-637X/774/2/134
- Goldsmith, P. F., Pineda, J. L., Langer, W. D., et al. 2016, *ApJ*, 824, 141. doi:10.3847/0004-637X/824/2/141
- Goldsmith, P. F., Velusamy, T., Li, D., et al. 2010, *ApJ*, 715, 1370. doi:10.1088/0004-637X/715/2/1370
- Goldsmith, P. F., Heyer, M., Narayanan, G., et al. 2008, *ApJ*, 680, 428. doi:10.1086/587166
- Green, G. M., Schlafly, E., Zucker, C., et al. 2019, *ApJ*, 887, 93. doi:10.3847/1538-4357/ab5362
- Habart, E., Boulanger, F., Verstraete, L., et al. 2004, *A&A*, 414, 531. doi:10.1051/0004-6361:20031659
- Heiles, C. 1969, *ApJ*, 156, 493. doi:10.1086/149983
- Hennebelle, P., Banerjee, R., Vázquez-Semadeni, E., et al. 2008, *A&A*, 486, L43. doi:10.1051/0004-6361:200810165
- Hollenbach, D. J. & Tielens, A. G. G. M. 1999, *Reviews of Modern Physics*, 71, 173. doi:10.1103/RevModPhys.71.173
- Koyama, H. & Inutsuka, S.-. ichiro . 2002, *ApJL*, 564, L97. doi:10.1086/338978
- Lenz, D., Hensley, B. S., & Doré, O. 2017, *ApJ*, 846, 38. doi:10.3847/1538-4357/aa84af
- Li, D. & Goldsmith, P. F. 2003, *ApJ*, 585, 823. doi:10.1086/346227
- Li, H., Li, D., Qian, L., et al. 2015, *ApJS*, 219, 20. doi:10.1088/0067-0049/219/2/20
- Loren, R. B., Plambeck, R. L., Davis, J. H., et al. 1981, *ApJ*, 245, 495. doi:10.1086/158825
- Lucas, R. & Liszt, H. 1998, *A&A*, 337, 246
- Mac Low, M.-M., Balsara, D. S., Kim, J., et al. 2005, *ApJ*, 626, 864. doi:10.1086/430122
- Mangum, J. G. & Shirley, Y. L. 2015, *PASP*, 127, 266. doi:10.1086/680323
- Milam, S. N., Savage, C., Brewster, M. A., et al. 2005, *ApJ*, 634, 1126. doi:10.1086/497123
- Narayanan, G., Heyer, M. H., Brunt, C., et al. 2008, *ApJS*, 177, 341. doi:10.1086/587786
- Navarrete, S., Pinargote, B. J., & Banda-Barragán, W. E. 2024, *Journal of Physics Conference Series*, 2796, 012005. doi:10.1088/1742-6596/2796/1/012005
- Nguyen, H., Dawson, J. R., Miville-Deschênes, M.-A., et al. 2018, *ApJ*, 862, 49. doi:10.3847/1538-4357/aac82b
- Ntormousi, E., Burkert, A., Fierlinger, K., et al. 2011, *ApJ*, 731, 13. doi:10.1088/0004-637X/731/1/13
- Orr, M. E., Pineda, J. L., & Goldsmith, P. F. 2014, *ApJ*, 795, 26. doi:10.1088/0004-637X/795/1/26
- Palmeirim, P., André, P., Kirk, J., et al. 2013, *A&A*, 550, A38. doi:10.1051/0004-6361/201220500
- Peek, J. E. G., Babler, B. L., Zheng, Y., et al. 2018, *ApJS*, 234, 2. doi:10.3847/1538-4365/aa91d3
- Penzias, A. A. 1975, *Atomic and Molecular Physics and the Interstellar Matter*, 373
- Ritchey, A. M., Federman, S. R., & Lambert, D. L. 2011, *ApJ*, 728, 36. doi:10.1088/0004-637X/728/1/36
- Scoville, N. Z., Yun, M. S., Clemens, D. P., et al. 1987, *ApJS*, 63, 821. doi:10.1086/191185
- Seifried, D., Beuther, H., Walch, S., et al. 2022, *MNRAS*, 512, 4765. doi:10.1093/mnras/stac607
- Shaw, G., Ferland, G. J., & Hubeny, I. 2017, *ApJ*, 843, 149. doi:10.3847/1538-4357/aa7747
- Sheffer, Y., Rogers, M., Federman, S. R., et al. 2007, *ApJ*, 667, 1002. doi:10.1086/520875

- Sheffer, Y., Rogers, M., Federman, S. R., et al. 2008, *ApJ*, 687, 1075. doi:10.1086/591484
- Snow, T. P. & McCall, B. J. 2006, *ARA&A*, 44, 367. doi:10.1146/annurev.astro.43.072103.150624
- Sobolev, V. V. 1957, *Soviet Ast.*, 1, 678
- Stahl, O., Casassus, S., & Wilson, T. 2008, *A&A*, 477, 865. doi:10.1051/0004-6361:20078747
- Tang, N.-Y., Zuo, P., Li, D., et al. 2020, *Research in Astronomy and Astrophysics*, 20, 077. doi:10.1088/1674-4527/20/5/77
- Valdivia, V., Hennebelle, P., Gérin, M., et al. 2016, *A&A*, 587, A76. doi:10.1051/0004-6361/201527325
- van der Tak, F. F. S., Black, J. H., Schöier, F. L., et al. 2007, *A&A*, 468, 627. doi:10.1051/0004-6361:20066820
- Vázquez-Semadeni, E., Gómez, G. C., Jappsen, A. K., et al. 2007, *ApJ*, 657, 870. doi:10.1086/510771
- Vázquez-Semadeni, E., Colín, P., Gómez, G. C., et al. 2010, *ApJ*, 715, 1302. doi:10.1088/0004-637X/715/2/1302
- Vázquez-Semadeni, E., Ryu, D., Passot, T., et al. 2006, *ApJ*, 643, 245. doi:10.1086/502710
- Wilson, T. L. 1999, *Reports on Progress in Physics*, 62, 143. doi:10.1088/0034-4885/62/2/002
- Xu, D. & Li, D. 2016, *ApJ*, 833, 90. doi:10.3847/1538-4357/833/1/90
- Xu, D., Li, D., Yue, N., et al. 2016, *ApJ*, 819, 22. doi:10.3847/0004-637X/819/1/22
- Zucker, C., Speagle, J. S., Schlafly, E. F., et al. 2020, *A&A*, 633, A51. doi:10.1051/0004-6361/201936145